

# Vertical $\alpha/\beta$ -Ga<sub>2</sub>O<sub>3</sub> phase junction nanorods array with graphene-silver nanowire hybrid conductive electrode for high-performance self-powered solar-blind photodetectors

C. Wu <sup>a, d</sup>, C. He <sup>a, d</sup>, D. Guo <sup>a, \*</sup>, F. Zhang <sup>b</sup>, P. Li <sup>c</sup>, S. Wang <sup>a</sup>, A. Liu <sup>a, \*\*</sup>, F. Wu <sup>a, \*\*\*</sup>, W. Tang <sup>c</sup>

<sup>a</sup> Center for Optoelectronics Materials and Devices, Key Laboratory of Optical Field Manipulation of Zhejiang Province, Department of Physics Zhejiang Sci-Tech University Hangzhou, 310018, China

<sup>b</sup> Guangxi Key Laboratory of Precision Navigation Technology, Application Guilin University of Electronic Technology Guilin, 541004, China

<sup>c</sup> State Key Laboratory of Information Photonics and Optical Communications, Laboratory of Information Functional Materials and Devices, School of Science, Beijing University of Posts and Telecommunications, Beijing, 100876, China



## ARTICLE INFO

### Article history:

Received 31 December 2019

Received in revised form

31 January 2020

Accepted 9 February 2020

Available online 21 February 2020

### Keywords:

$\alpha/\beta$ -Ga<sub>2</sub>O<sub>3</sub> junction  
Vertical nanorods  
Graphene-Ag NWs

## ABSTRACT

Gallium oxide semiconductor, with a bandgap energy of 4.9 eV, is regarded as a hopeful candidate for next-generation solar-blind photodetectors. However, the construction of photodetector based on Ga<sub>2</sub>O<sub>3</sub> pn junction is still challengeable due to immature doping technology of p-Ga<sub>2</sub>O<sub>3</sub>. By considering the small lattice mismatch ( $< 3\%$ ) and similar band gap structure of  $\alpha$ -Ga<sub>2</sub>O<sub>3</sub> and  $\beta$ -Ga<sub>2</sub>O<sub>3</sub>, a well-designed solar-blind photodetector was built, based on vertical  $\alpha/\beta$ -Ga<sub>2</sub>O<sub>3</sub> junction nanorod arrays (NRAs) with a graphene-silver nanowires (Ag NWs) hybrid top electrode. Thanks to the high conductivity and optical transmittance of graphene-Ag NWs top electrode, the photodetector based on  $\alpha/\beta$ -Ga<sub>2</sub>O<sub>3</sub> junction NRAs displayed excellent photoelectric performance. Meanwhile, the matched band structure of II type formed at the interface of  $\alpha/\beta$ -Ga<sub>2</sub>O<sub>3</sub> junction promoted the automatic separation of photogenerated carriers and their transfer to the corresponding electrodes. A fast photoresponse time of 0.54 s, a high light-to-dark ratio about 2000, and a high rejection ratio ( $R_{254}/R_{365}$ ) of  $2.7 \times 10^3$  under the zero bias, were realized. The excellent photoelectrical performance of  $\alpha/\beta$ -Ga<sub>2</sub>O<sub>3</sub> junction photodetector even in vacuum environment forecasts its potential application in some low air density fields, such as missile early warning and tracking and ozone hole monitoring.

© 2020 Elsevier Ltd. All rights reserved.

## 1. Introduction

Gallium oxide (Ga<sub>2</sub>O<sub>3</sub>) semiconductor, with a bandgap energy of 4.9 eV, is regarded as a hopeful candidate for next-generation solar-blind photodetectors [1–3]. Owing to their high photosensitivity and high accurate alarm rate, Ga<sub>2</sub>O<sub>3</sub>-based solar-blind photodetectors attract much attention in military and civilian fields, such as fire early warning and monitoring, solar-blind communication, missile early warning and tracking, ultraviolet monitoring, ozone hole detecting, and so on [4–7]. For meeting the demand of the

photodetectors toward more energy-saving, miniaturization, and high efficiency [8–11], Ga<sub>2</sub>O<sub>3</sub> self-powered photodetectors, based on the Schottky junctions [12,13], heterojunctions [14–17], and pn junctions [18–21], have been developed rapidly, which can work continuously without external power supply. Although these photodetectors exhibit appropriate photoelectric performance, there are still some constraints that affect the further improvement of device performance: (1) The low light transmission of the metal upper electrode and the complex preparation process of Schottky contact for Schottky-type devices [22]; (2) Photosensitivity to the nonsolar-blind region on account of the narrower bandgap of the heterojunction materials and the lattice mismatch for heterojunction-type and pn junction-type devices [23–27]. For example, according to our previous report, the self-powered photodetector based on GaN/Sn:Ga<sub>2</sub>O<sub>3</sub> pn junction exhibited an ultrahigh responsivity to the solar-blind light (ultraviolet C, 200–280 nm) [28], but it was also photosensitive to the ultraviolet

\* Corresponding author.

\*\* Corresponding author.

\*\*\* Corresponding author.

E-mail addresses: dyguo@zstu.edu.cn (D. Guo), liuaiping1979@gmail.com (A. Liu), wfm@zstu.edu.cn (F. Wu).

<sup>d</sup> These authors contributed equally.

A (320–420 nm) with a maximum wavelength of 370 nm. In order to further improve the device performance, an ideal homogenous *pn* junction structure for  $\text{Ga}_2\text{O}_3$  solar-blind photodetectors was suggested [29,30]. However, the immature doping technology of *p*- $\text{Ga}_2\text{O}_3$  is still the barrier for avoiding the self-compensation process [31–34].

Considering the various crystal structure of  $\text{Ga}_2\text{O}_3$  ( $\alpha$ ,  $\beta$ ,  $\gamma$ ,  $\delta$ ,  $\epsilon$ ), a desirable solution to solve the problems existed in the heterojunction photodetectors is to construct  $\alpha\text{-}\text{Ga}_2\text{O}_3/\beta\text{-}\text{Ga}_2\text{O}_3$  junction because  $\alpha\text{-}\text{Ga}_2\text{O}_3$  and  $\beta\text{-}\text{Ga}_2\text{O}_3$  have small lattice mismatch (<3%) and similar bandgap [35–41], which is useful for promoting automatic separation of photogenerated carriers at the  $\alpha\text{-}\text{Ga}_2\text{O}_3$  junction and their further transfer to the corresponding electrodes [42,43]. Herein, we propose a self-powered solar-blind photodetector based on vertical  $\alpha\text{-}\text{Ga}_2\text{O}_3$  junction NRAs. The one-dimensional vertical NRAs can provide large surface, low optical reflectivity, and efficient coupling with incident light for photodetector [44,45]. Furthermore, a monolayer graphene-silver nanowires (graphene-Ag NWs) hybrid film with high electric conductivity and optical transparency is used as a top electrode of the solar-blind photodetector. The  $\alpha\text{-}\text{Ga}_2\text{O}_3$  junction NRAs photodetector with graphene-Ag NWs hybrid top electrode shows a responsivity ( $R$ ) of 0.26 mA/W within 0.54 s under the irradiation of 254 nm light at 0 V bias. The built-in electric field of  $\alpha\text{-}\text{Ga}_2\text{O}_3$  phase junction promotes the separation of photo-generated carriers, which significantly enhances the spectral selectivity and the rejection ratio ( $R_{254}/R_{365}$ ) of the junction photodetector up to  $2.7 \times 10^3$  without significant degradation of the performance even in a vacuum environment. This indicates its potential application as the commercialized space warning detector.

## 2. Method

### 2.1. Preparation of $\alpha\text{-}\text{Ga}_2\text{O}_3$ NRAs

The FTO substrates were placed in  $\text{Ga}(\text{NO}_3)_3 \cdot 9\text{H}_2\text{O}$  and heated at 150 °C for a night to get  $\text{GaOOH}$  NRAs. Then the as-prepared  $\text{GaOOH}$  NRAs were converted into the  $\alpha\text{-}\text{Ga}_2\text{O}_3$  after annealed at 400 °C for 4 h and annealed at 700 °C for 10 min. After the growth, the sample was washed by DI water and dried in air at 80 °C. The detailed process has been described in our previous report [7,46–49].

### 2.2. Device fabrication

A 0.5 cm × 1 cm graphene film grown on Cu foil was transferred onto  $\alpha\text{-}\text{Ga}_2\text{O}_3$  NRAs by the wet transfer method. The CVD grown Cu/graphene film was purchased from Nanjing Muke Nano Technology co., Ltd. Then, 200 μL of 0.4 mg/mL Ag NWs alcoholic solution was dropped onto the NRAs as an upper electrode with the aid of a shadow mask. Finally, a small circular silver electrode (0.05 × 0.05 cm<sup>2</sup>) is deposited on the corner of the graphene-silver nanowires hybrid film as the connection point of the external circuit.

### 2.3. Characterization and measurement

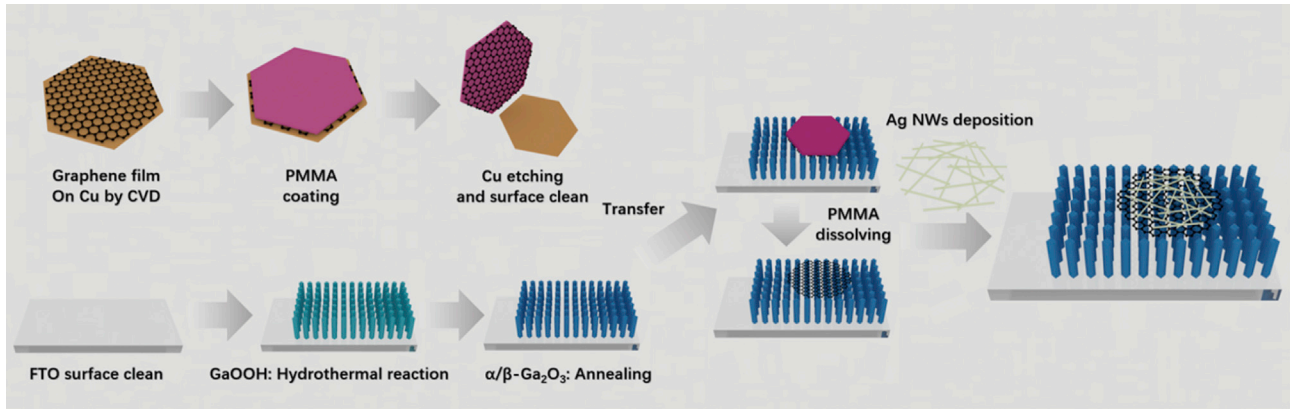
The morphologies of  $\alpha\text{-}\text{Ga}_2\text{O}_3$  NRAs and graphene-Ag NWs were observed by a scanning electron microscope (SEM, JSM-5610LV). A Hitachi U-3900 UV-vis spectrophotometer was used to test the transmittance of the sample. Current-voltage (*I*-V) characteristics and time-dependent photoresponse (*I*-T) of the photodetector were measured by Keithley 4200 device.

## 3. Results and discussion

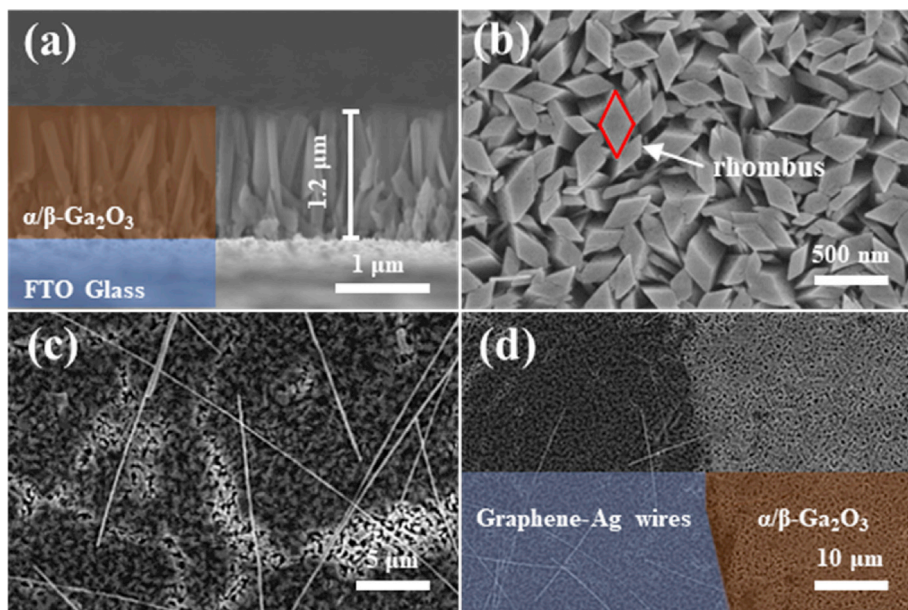
The fabrication process of  $\alpha\text{-}\beta\text{-}\text{Ga}_2\text{O}_3$  phase junction NRAs based self-powered solar-blind photodetector with graphene-Ag NWs hybrid film top electrode is schematically illustrated in Fig. 1. First,  $\alpha\text{-}\beta\text{-}\text{Ga}_2\text{O}_3$  phase junction NRAs were grown on FTO substrates by hydrothermal method, calcination, and followed by post-annealing treatment at 700 °C for 10 min. The detailed process has been described in our previous report. Second, in order to achieve a large-detective-area, a 0.5 × 1 cm<sup>2</sup> monolayer graphene film grown by CVD was transferred onto  $\alpha\text{-}\beta\text{-}\text{Ga}_2\text{O}_3$  NRAs by the wet transfer method. Then, an alcoholic solution contained with a few silver nanowires is dropped on graphene film with the aid of a shadow mask. Finally, a small circular silver electrode (0.05 × 0.05 cm<sup>2</sup>) is deposited on the corner of the graphene-silver nanowires hybrid film as the connection point of the external circuit.

Fig. 2a shows the morphology of the NRAs, which present an average length of about 1.2 μm grown vertically on FTO substrates. The NRAs arrange tightly and exhibit the diamond-shaped tip with the average diagonal lengths from 150 nm to 300 nm (Fig. 2b) due to the orthorhombic structure of  $\text{GaOOH}$  NRAs of the raw material. The top view FESEM images of the graphene- Ag NWs hybrid film fabricated on  $\alpha\text{-}\beta\text{-}\text{Ga}_2\text{O}_3$  NRAs is presented in Fig. 2c and d. The hybrid film covers the top of the  $\alpha\text{-}\beta\text{-}\text{Ga}_2\text{O}_3$  NRAs smoothly and tightly, meaning that good contact has been formed. However, inevitable cracks and holes appear in the monolayer graphene film during the wet transfer process. The introduction of Ag NWs in the monolayer graphene film can provide a two-dimensional conducting channel to ensure the high conductivity of the top electrode. The characterization of monolayer graphene film is also shown in the supporting information. The Raman spectrum of the as-grown graphene shows 2D and G bands located at 2675 cm<sup>-1</sup> and 1583 cm<sup>-1</sup> and the D bands at around 1383 cm<sup>-1</sup> due to the existence of defects in the graphene film (Fig. S1a). The peak intensity ration  $I_G/I_{2D} < 0.5$  indicates the nature of the monolayer graphene film [50]. The diameter of the Ag NWs used here is around 150 nm, and their lengths reach several tens to hundreds of micrometers (Fig. S1b).

The solar-blind photoelectric performance of  $\alpha\text{-}\beta\text{-}\text{Ga}_2\text{O}_3$  junction NRAs photodetector was investigated under the irradiation of ultraviolet light with a wavelength of 254 nm. The *I*-V curves of the photodetector are nonlinear and asymmetric (Fig. 3a), which display an off-state current at the reverse bias and an on-state current at the forward bias. At the bias of 0 V, the current is 1.72 nA in the dark and increases to 211.07 nA under a 254 nm light illumination with the intensity of 3000 μW/cm<sup>2</sup>, exhibiting a self-powered characteristic. The typical photovoltaic characteristics are clearly observed from the enlarged *I*-V curves of  $\alpha\text{-}\beta\text{-}\text{Ga}_2\text{O}_3$  phase junction photodetector near zero bias (the inset of Fig. 3a). The open-circuit voltage and the short-circuit current under 254 nm light (intensity of 1600 μW/cm<sup>2</sup>) are 0.01 V and 8.71 nA, respectively, which further increase with the increasing light intensity. In order to evaluate the effect of light intensity on the photodetector, *I*-*t* measurements are performed under 254 nm light with different light intensity (Fig. 3b). Notably, the photocurrent increases linearly from 12.21 nA to 211.07 nA as the light intensity increases from 100 to 3000 μW/cm<sup>2</sup>. At a higher light intensity, a higher photocurrent is originated from more photo-generated electron-hole pairs produced by the light absorption layer. The responsivity ( $R$ ) is usually regarded as an important parameter to evaluate the sensitivity of the photodetector, which can be calculated by formula  $R = (I_{photo} - I_{dark})/(PS)$ , where  $I_{photo}$  and  $I_{dark}$  is the photocurrent and dark current, respectively,  $P$  is the supplied light intensity, and  $S$  is the effective area of the photodetector. The  $R$  of the photodetector decreases from 0.26 mA/W to



**Fig. 1.** Scheme of  $\alpha/\beta\text{-Ga}_2\text{O}_3$  NRAs hybrids-based photodetector with graphene-Ag NWs hybrid top electrode.



**Fig. 2.** (a) The cross-section of  $\beta\text{-Ga}_2\text{O}_3$  NRAs grown on the FTO substrate; (b) The top views of SEM images of  $\alpha/\beta\text{-Ga}_2\text{O}_3$  NRAs; (c) and (d) The SEM and edge view of graphene-Ag NWs top electrode.

0.14 mA/W as the light intensity increases from 100 to 3000  $\mu\text{W}/\text{cm}^2$ , as shown in Fig. 3c, owing to the increased possibility of recombination of photogenerated electron-hole pairs at a higher intensity light [58]. The detection ability to weak light is another important index for a photodetector, which is usually measured by detectivity ( $D$ ). The  $D$  decreases with the increase of light intensity and achieves a maximum value of  $2.8 \times 10^9 \text{ cm Hz}^{1/2} \text{ W}^{-1}$  at the light intensity of 100  $\mu\text{W}/\text{cm}^2$ , as shown in Fig. 3d. To further assess the photoelectricity performance of the photodetector, the effect of bias voltage on the photoresponses of  $\alpha/\beta\text{-Ga}_2\text{O}_3$  NRAs-based photodetector is studied, and the curves are shown in Fig. 3d. Owing to the faster drift velocity and more carriers releasing from oxygen vacancy traps at higher bias, the dark current increases rapidly from 1 nA to 2  $\mu\text{A}$  with the increase of voltage from 0 to 1 V. Meanwhile, the photocurrent also increases with the increasing applied bias due to the more effective separation of photogenerated electron-hole pair. For calculating the response speed of the photodetector, the fitting curve is shown in Fig. 3f. The constant  $\tau_1$  is related to the rapid change of the carrier concentration when the UV light is turned on/off, and  $\tau_2$  is related to carrier trapping and

releasing due to the oxygen vacancy defects in the nanorods. The  $\alpha/\beta\text{-Ga}_2\text{O}_3$  phase junction photodetector shows a fast response speed with a rise time of 0.54 s ( $\tau_{r1}$ ). To further evaluate the spectral selectivity of the device, the performance of the  $\alpha/\beta\text{-Ga}_2\text{O}_3$  NRAs photodetector under 365 nm light irradiation are measured (Fig. S2). The rejection ratio ( $R_{254}/R_{365}$ ) of the device at 0 V bias can reach up to  $2.7 \times 10^3$ , which hints at a high spectral selectivity of the solar-blind region. The performance is comparable to many reported  $\text{Ga}_2\text{O}_3$ -based photodetectors listed in Table 1.

The effect of graphene-Ag NWs top electrode on the performance of  $\alpha/\beta\text{-Ga}_2\text{O}_3$  NRAs photodetector is also probed into. The photodetector with the monolayer graphene as top electrode shows the lowest dark current of 0.23 nA, as shown in Fig. 4a, because the monolayer graphene with inevitable cracks and holes only presents poor electrical conductivity. Compared with the monolayer graphene electrode, the dark current of the photodetector with the graphene-Ag NWs hybrid electrode is 1.01 nA, exhibiting an improved conductivity. Although the quality of CVD-growth graphene is outstanding, it is reported that the sheet resistance of the transferred CVD-grown monolayer graphene film

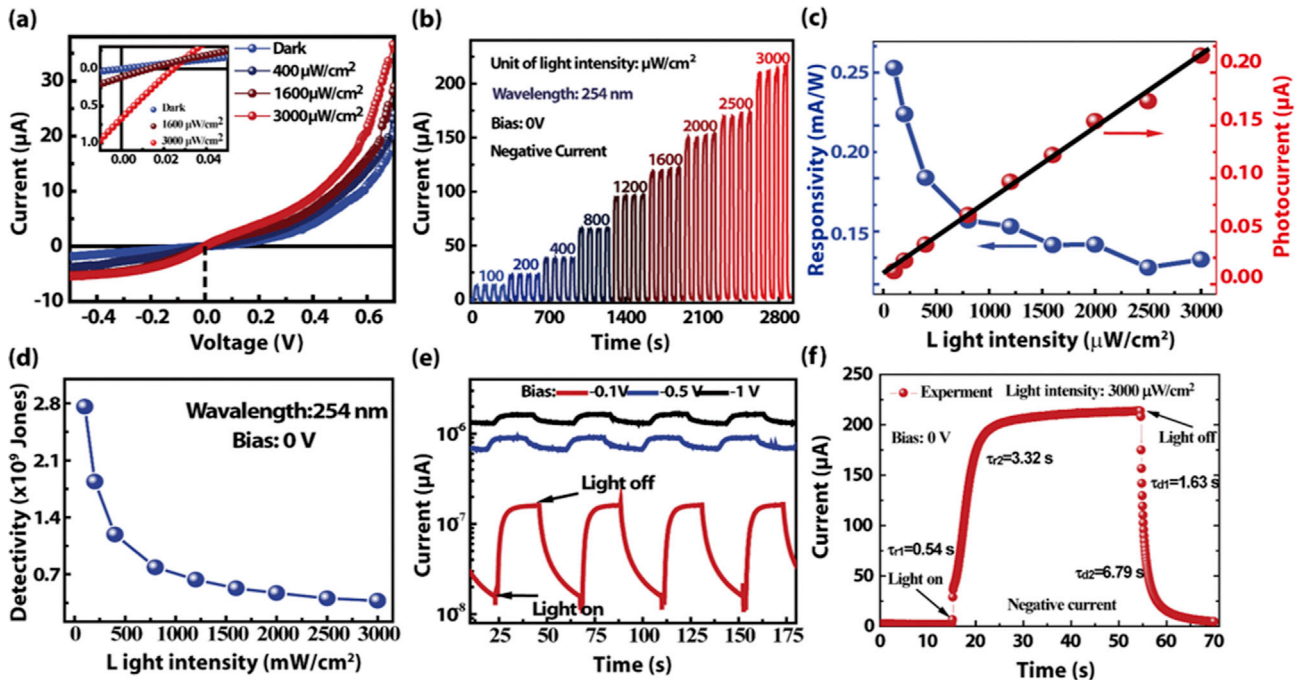


**Fig. 3.** (a) I–V characteristic curve of the  $\alpha/\beta\text{-Ga}_2\text{O}_3$  NRAs photodetector under dark and 254 nm illumination with various light intensities, the inset is the I–V enlarged curves near zero bias; (b) Time-dependent photoresponse of the photodetector under zero bias and 254 nm light with various light intensities; (c) Photocurrent and responsivity as a function of the light intensity; (d) Detectivity as a function of the light intensity; (e) Time-dependent photoresponse of the photodetector under various bias with 254 nm LED light illumination; (f) enlarged view of the rise/decay edges and the corresponding exponential fitting.

( $2100 \Omega \text{ sq}^{-1}$ ) is too high to use as an electrode [51,52]. Thus, it is required to improve the conductivity of the transferred graphene without sacrifice optical transparency. Compared with the monolayer graphene electrode, graphene-Ag NWs hybrid electrode exhibits excellent electron transport properties. The improved electrical conductivity of the hybrid electrode could be originated from the two factors (1) Synergy from percolation through the Ag NWs, bridge graphene cracks, and polydomains; (2) Graphene layer eliminate of open space between nonconnected Ag NWs [53–57]. Under the light intensity of  $3000 \mu\text{W}/\text{cm}^2$ , the photocurrent of the photodetector with the graphene-Ag NWs top electrode exhibits the highest photocurrent of  $211.07 \text{nA}$ , which is tenfold higher than that obtained from the photodetector with monolayer graphene electrode. The transmittance spectra of different transparent electrodes are shown in Fig. 4b. The optical transmittance of the monolayer graphene and Ag NWs are 93.6% and 84.1% at 250 nm, respectively, while those of the bilayer graphene and monolayer graphene-Ag NWs film are 89.5% and 92.1%, respectively. The

photograph of the device inserted in Fig. 4b further confirms its transparency. Tradeoff the conductivity and transmittance, the graphene-Ag NWs film is suitable for the top electrode. Additionally, the internal electric field induced by the  $\alpha/\beta\text{-Ga}_2\text{O}_3$  phase junction also favors the automatic separation of photogenerated carriers, and therefore, improves the performance of the photodetector. Fig. 4c displays the response of the three prototype devices under 254 nm light illumination, with the light intensity of  $3000 \mu\text{W}/\text{cm}^2$  at 0 V. Obviously, the phase junction NRAs device demonstrates an enhancement in the photoresponse current ( $\sim 21 \text{nA}$ ) in comparison to the  $\alpha\text{-Ga}_2\text{O}_3$  NRAs ( $36 \text{nA}$ ) and  $\beta\text{-Ga}_2\text{O}_3$  NRAs ( $121 \text{nA}$ ). For a more detailed study, the rise and decay processes of the photoresponse are demonstrated in Fig. 4d. The rise time ( $\tau_{r1}$ ) of  $\alpha/\beta\text{-Ga}_2\text{O}_3$  phase junction photodetector is about  $0.54 \text{s}$ , which is faster than those of  $\alpha\text{-Ga}_2\text{O}_3$  ( $1.24 \text{s}$ ) and  $\beta\text{-Ga}_2\text{O}_3$  ( $1.12 \text{s}$ ) devices, indicating that the construction of  $\alpha/\beta\text{-Ga}_2\text{O}_3$  phase junction effectively promotes the response speed. In order to explain this phenomenon, the energy band diagram of the  $\alpha/\beta\text{-}$

**Table 1**  
Comparison of the photoresponse parameters of the  $\alpha/\beta\text{-Ga}_2\text{O}_3$  junction nanorods solar-blind photodetector under zero bias from this work and other previously reported  $\text{Ga}_2\text{O}_3$  devices.

Photodetector	Wavelength (nm)	Responsivity (mA/W)	$I_{\text{photo}}/I_{\text{dark}}$	Rejection Ratio	Ref
Au// $\beta\text{-Ga}_2\text{O}_3$ Nanowires	270	0.01 (0 V)	$1 \times 10^3$	$\sim 38(R_{258}/R_{400})$	[22]
$\beta\text{-Ga}_2\text{O}_3/\text{NSTO}$	254	2.6 (0 V)	20	1	[15]
$\text{Ga}_2\text{O}_3/\text{ZnO}$	254	9.7 (0 V)	$1 \times 10^4$	$690(R_{254}/R_{400})$	[16]
p-GaN/n-Ga <sub>2</sub> O <sub>3</sub>	254	28.4(0 V)	74	$152(R_{254}/R_{400})$	[21]
diamond// $\beta\text{-Ga}_2\text{O}_3$	270	0.2 (0 V)	242	$135(R_{254}/R_{400})$	[53]
$\text{Ga}_2\text{O}_3/\text{SiC}$	254	0.7 (0 V)	37	1	[54]
$\text{Ga}_2\text{O}_3\text{Ga:ZnO}$	254	0.76 (0 V)	106	$\sim 100(R_{254}/R_{365})$	[17]
GaN/Sn:Ga <sub>2</sub> O <sub>3</sub>	254	$3.05 \times 10^3$ (0 V)	$6 \times 10^*$	$5.9 \times 10^3(R_{254}/R_{400})$	[35]
Si/Ga <sub>2</sub> O <sub>3</sub>	254	$3.7 \times 10^5$ (3V)	904	$\sim 10^3(R_{254}/R_{365})$	[34]
Graphene/Ga <sub>2</sub> O <sub>3</sub> /graphene	254	9.66(0 V)	$1 \times 10^4$	1	[59]
ZnO/Ga <sub>2</sub> O <sub>3</sub> core-shell	254	$1.3 \times 10^3$ (-6V)	$1 \times 10^6$	1	[60]
$\alpha/\beta\text{-Ga}_2\text{O}_3$	254	0.26 (0 V)	127	$2.7 \times 10^3(R_{254}/R_{365})$	this work

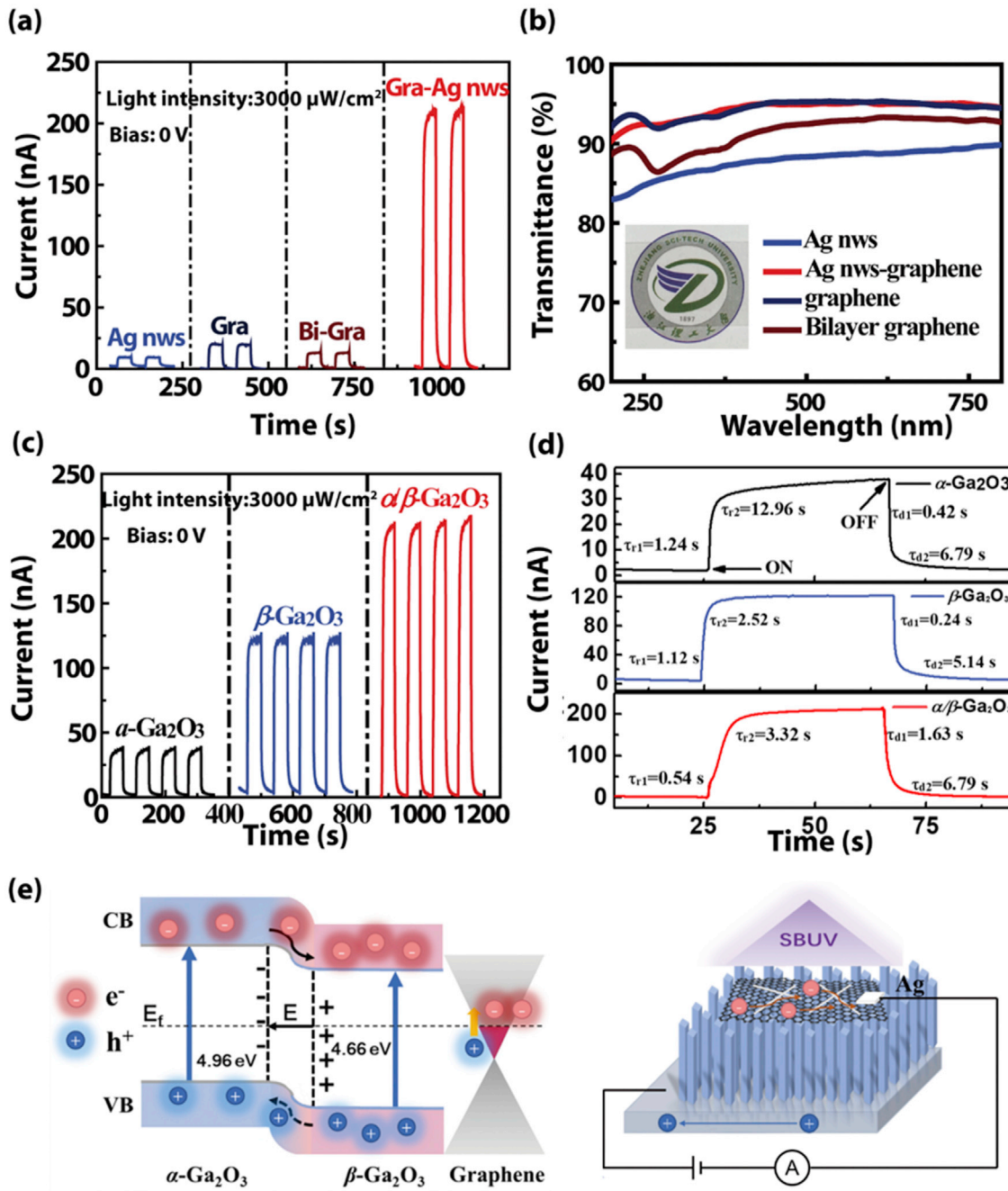


**Fig. 4.** (a) Time-dependent photoresponse of the  $\alpha/\beta\text{-Ga}_2\text{O}_3$  phase junction photodetector with different top electrodes under zero bias and 254 nm light; (b) Transmittance of different top electrodes; (c) Time-dependent photoresponse of the  $\alpha\text{-Ga}_2\text{O}_3$ ,  $\beta\text{-Ga}_2\text{O}_3$  and  $\alpha/\beta\text{-Ga}_2\text{O}_3$  phase junction photodetector under zero bias and 254 nm light; (d) enlarged view of the rise/decay edges and the corresponding exponential fitting; (e) illustrations of the proposed band alignment of the  $\alpha/\beta\text{-Ga}_2\text{O}_3$  phase junction and the charge carrier transport route.

$\text{Ga}_2\text{O}_3$  junction is given in Fig. 4e. The bandgap energies of  $\alpha\text{-Ga}_2\text{O}_3$  and  $\beta\text{-Ga}_2\text{O}_3$  are 4.96 and 4.66 eV [7], respectively. Both the conduction band potential ( $E_c$ ) and the valence band potential ( $E_v$ ) of  $\alpha\text{-Ga}_2\text{O}_3$  are more positive than those of  $\beta\text{-Ga}_2\text{O}_3$ , exhibiting a  $\Pi$  type of band structure. Because of the potential difference of  $\alpha\text{-Ga}_2\text{O}_3$  and  $\beta\text{-Ga}_2\text{O}_3$ , the photogenerated electron-hole pairs can effectively be separated under the illumination. As a result, the photogenerated holes and electrons transfer to  $\alpha\text{-Ga}_2\text{O}_3$  and  $\beta\text{-Ga}_2\text{O}_3$  NRAs, respectively.

By taking advantage of self-powered characteristic and ultra-sensitive spectral selectivity, our proposed solar-blind

photodetector shows the potential application in space detection and warning. However, for space warning, photodetectors are required to work at a million meters altitude and even outer space where the air is ultralow dense. For simulating the performance of the photodetector working in outer space environment, the measurements were carried out in vacuum (~1 Pa) under 254 nm light illumination at 0 V bias. As shown in Fig. 5a and b, the  $\alpha/\beta\text{-Ga}_2\text{O}_3$  NRAs junction photodetector demonstrates an ultralow dark current of 1.36 pA and a photocurrent of 4.73 nA, which are 100 times less than that in atmospheric conditions. The photoresponse time is 0.16 s ( $t_{r1}$ ) in a vacuum, which is an order of magnitude faster than

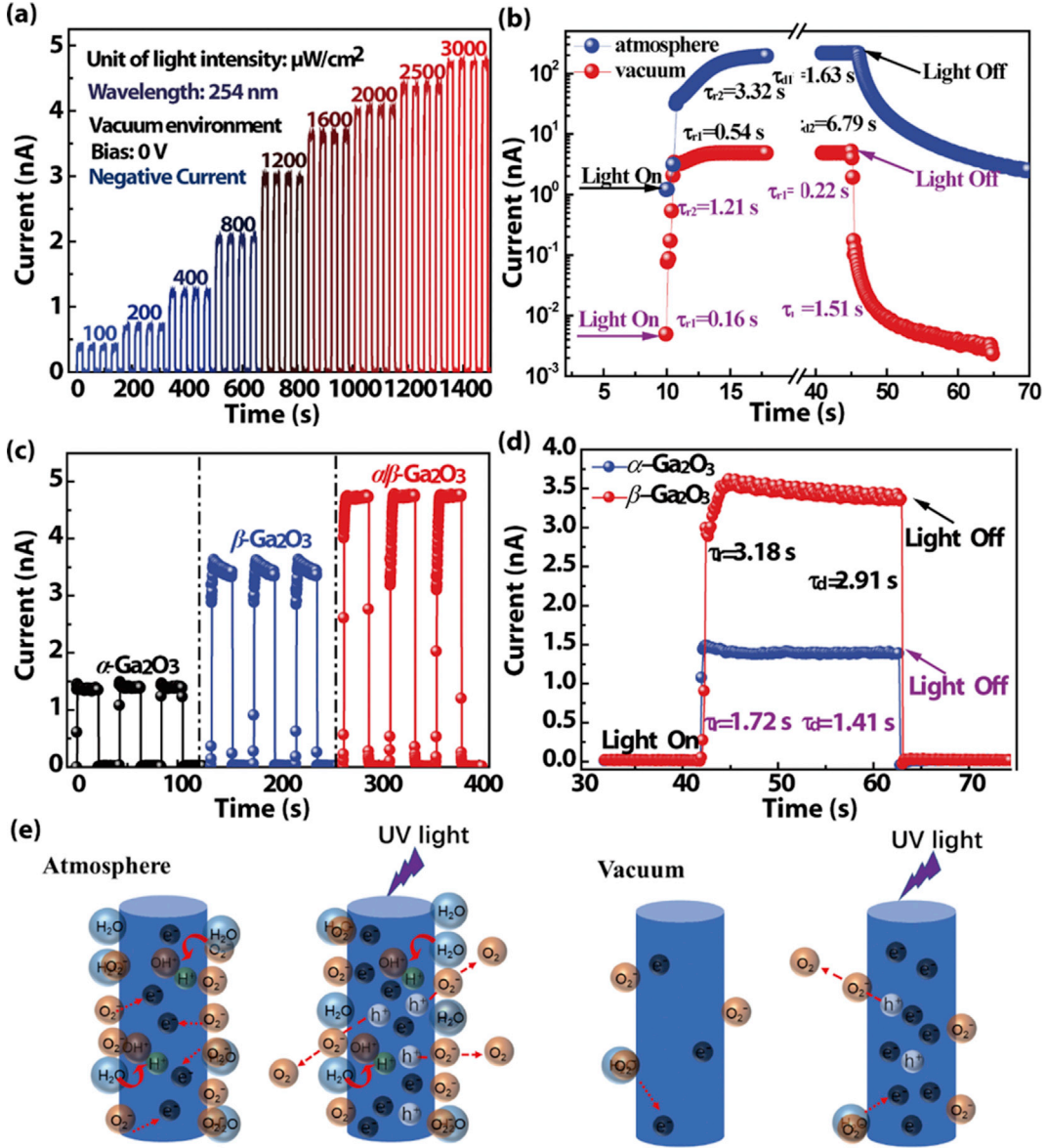


**Fig. 5.** (a) Time-dependent photoresponse of the photodetector under zero bias and 254 nm light with various light intensities in vacuum environment; (b) Time-dependent photoresponse of the  $\alpha/\beta\text{-Ga}_2\text{O}_3$  phase junction photodetector in vacuum and air environment under zero bias and 254 nm light; (c) Time-dependent photoresponse of the  $\alpha\text{-Ga}_2\text{O}_3$ ,  $\beta\text{-Ga}_2\text{O}_3$  and  $\alpha/\beta\text{-Ga}_2\text{O}_3$  phase junction photodetector under 254 nm light; (d) enlarged view of the rise/decay edges and the corresponding exponential fitting; Schemas of oxygen and water molecules on surface of  $\alpha/\beta\text{-Ga}_2\text{O}_3$  NRAs at (e) vacuum and (f) air in the dark and under UV illumination.

that in the atmosphere. Additionally, the photogenerated electron-hole pairs can still effectively be separated under illumination in a vacuum. The photodetector holds an enhanced photocurrent and a fast response speed than the pure  $\alpha\text{-Ga}_2\text{O}_3$  and  $\beta\text{-Ga}_2\text{O}_3$  NRAs device. The photoresponse of the device will be affected by adsorption and desorption of oxygen molecules on the  $\alpha/\beta\text{-Ga}_2\text{O}_3$  NRAs surface. In the atmosphere, owing to the large surface-to-volume ratio of NRAs, a large amount of  $\text{O}_2$  will be adsorbed on the surface of  $\alpha/\beta\text{-Ga}_2\text{O}_3$  NRAs, which decreases the carrier density and leads to an upward band bending. The adsorbed  $\text{O}_2$  is ionized to  $\text{O}_2^-$  by water molecules and released electrons, which significantly increases the conductivity of the device. On the contrary, in a vacuum, less  $\text{O}_2$  is adsorbed and ionized on the surface, and the energy bands are less bent. Hence, the device in a vacuum shows a lower current and a shorter response time. Owing to the great performance of the  $\alpha/\beta\text{-Ga}_2\text{O}_3$  NRAs junction photodetector in a vacuum, the device shows

wide potential applications in some fields, such as missile early warning and tracking and ozone hole monitoring, which needs to work in low air density.

#### 4. Conclusion

In summary, high-performance self-powered solar-blind photodetectors based on the  $\alpha/\beta\text{-Ga}_2\text{O}_3$  junction NRAs with highly conductive and transparent graphene-Ag NWs as a top conductive electrode was proposed. Compared with a conventional metal electrode, the graphene-Ag NWs electrode with tight conduction with the  $\alpha/\beta\text{-Ga}_2\text{O}_3$  showed excellent electrical conductivity and optical transparency and improved the efficiency of separation and transfer of photogenerated carriers. The well-designed photodetector showed an enhanced performance, namely a high responsivity of 0.26 mA/W, a high  $I_{\text{dark}}/I_{\text{photo}}$  ratio of  $2.1 \times 10^2$ , large

detectivity of  $2.8 \times 10^9$  Jones with a high rejection ratio ( $R_{254}/R_{365}$ ) of  $2.7 \times 10^3$  even without external power. Such excellent photoelectric performance of self-powered solar-blind photodetector has potential application prospects in ultraviolet monitoring, UV communication, and space detection.

## Credit author statement

**Daoyou Guo, Fengmin Wu and Weihua Tang:** Conceptualization, Methodology, **Chao Wu** and **Chenran He:** Investigation, Writing- Original draft preparation. **Shunli Wang** and **Daoyou Guo:** Supervision. **Fabi Zhang, Peigang Li** and **Aiping Liu:** Writing-Reviewing and Editing. **Daoyou Guo, Peigang Li** and **Fengmin Wu:** Project administration, Funding acquisition.

## Declaration of Competing Interest

The authors declare no conflict of interest.

## Acknowledgements

This work was supported by the National Natural Science Foundation of China (No. 61704153, 61764001, 61774019), Zhejiang Public Service Technology Research Program/Analytical Test (LGC19F040001), Guangxi Science and Technology Base and Talent Special Project (AD18281084), Open Fund of Key Laboratory of Cognitive Radio and Information Processing Ministry of Education (Guilin University of Electronic Technology), and Fundamental Research Funds of Zhejiang Sci-Tech University (2019Q061, 2019Q067).

## Appendix A. Supplementary data

Supplementary data to this article can be found online at <https://doi.org/10.1016/j.mtphys.2020.100193>.

## References

- [1] S.J. Pearson, J.C. Yang, P.H. Cary, F. Ren, J. Kim, M.J. Tadje, M.A. Mastro, *Appl. Phys. Rev.* 5 (2018): 011301.
- [2] M. Higashiwaki, G.H. Jessen, *Appl. Phys. Lett.* 112 (2018): 060401.
- [3] Z. Galazka, *Semicond. Sci. Technol.* 33 (2018): 113001.
- [4] D.Y. Guo, X.L. Zhao, Y.S. Zhi, W. Cui, Y.Q. Huang, Y.H. An, P.G. Li, Z.P. Wu, W.H. Tang, *Mater. Lett.* 164 (2016) 364.
- [5] D.Y. Guo, P.G. Li, Z.P. Wu, W. Cui, X.L. Zhao, M. Lei, L. Li, W.H. Tang, *Sci. Rep.* 6 (2016) 24190.
- [6] D.Y. Guo, Y.P. Qian, Y.L. Su, H.Z. Shi, P.G. Li, J.T. Wu, S.L. Wang, C. Cui, W.H. Tang, *AIPI Adv.* 7 (2017): 065312.
- [7] S.L. Wang, H.L. Sun, Z. Wang, X. Zeng, G. Ungar, D.Y. Guo, J. Shen, P.G. Li, A. Liu, C. Li, W.H. Tang, *J. Alloys Compd.* 787 (2019) 133.
- [8] H.M. Wang, D. Li, W. Zhong, L. Xu, T. Jiang, Z.L. Wang, *ACS Appl. Mater. Interfaces* 11 (37) (2019) 34251–34257.
- [9] Q.L. Ouyang, X.L. Feng, S.Y. Kuang, N. Panwar, P.Y. Song, C.B. Yang, G. Yang, X.Y. Hemu, G. Zhang, H.S. Yoon, J.P. Tam, B. Liedberg, G. Zhu, K.T. Yong, Z.L. Wang, *Nano energy* 62 (2019) 610–619.
- [10] X. Wang, Y. Cui, T. Li, M. Lei, J. Li, Z. Wei, *Adv. Opt. Mater.* 7 (2018): 1801274.
- [11] J. Wei, F. Guo, X. Wang, K. Xu, M. Lei, Y. Liang, Y. Zhao, D. Xu, *Adv. Mater.* 30 (2018): e1805153.
- [12] D.Y. Guo, Z.P. Wu, Y.H. An, X.C. Guo, X.L. Chu, C.L. Sun, L.H. Li, P.G. Li, W.H. Tang, *Appl. Phys. Lett.* 105 (2014): 023507.
- [13] T. He, X.D. Zhang, X.Y. Ding, C. Sun, Y.K. Zhao, Q. Yu, J.Q. Ning, R.X. Wang, G.H. Yu, S.L. Lu, K. Zhang, X.P. Zhang, B.S. Zhang, *Adv. Optical Mater.* (2019) 1801563.
- [14] M. Chen, B. Zhao, G. Hu, X. Fang, H. Wang, L. Wang, J. Luo, X. Han, X. Wang, C. Pan, Z.L. Wang, *Adv. Funct. Mater.* 28 (2018): 1706379.
- [15] D.Y. Guo, H. Liu, P.G. Li, Z.P. Wu, S.L. Wang, C. Cui, C. Li, W.H. Tang, *ACS Appl. Mater. Interfaces* 9 (2017) 1619.
- [16] B. Zhao, F. Wang, H. Chen, L. Zheng, L. Su, D. Zhao, X. Fang, *Adv. Funct. Mater.* 27 (2017): 1700264.
- [17] Z.P. Wu, L. Jiao, X.L. Wang, D.Y. Guo, W. Li, L. Li, F. Huang, W.F. Tang, *J. Mater. Chem. C* 5 (2017) 8688.
- [18] B. Zhao, F. Wang, H.Y. Chen, L.X. Zheng, L.X. Su, D.X. Zhao, X.S. Fang, *Adv. Funct. Mater.* 27 (2017): 1700264.
- [19] Y.C. Chen, Y.J. Lu, C.N. Lin, Y.Z. Tian, C.J. Gao, L. Dong, C.X. Shan, *J. Mater. Chem. C* 6 (2018) 5727.
- [20] B. Zhao, F. Wang, H. Chen, Y. Wang, M. Jiang, X. Fang, D. Zhao, *Nano Lett.* 15 (2015) 3988.
- [21] P.G. Li, H.Z. Shi, K. Chen, D.Y. Guo, W. Cui, Y. Zhi, S.L. Wang, Z.P. Wu, Z. Chen, W.H. Tang, *J. Mater. Chem. C* 5 (2017) 10562.
- [22] X. Chen, K. Liu, Z. Zhang, C. Wang, B. Li, H. Zhao, D. Zhao, D. Shen, *ACS Appl. Mater. Interfaces* 8 (2016) 4185.
- [23] J. Yu, Z. Nie, L. Dong, L. Yuan, D. Li, Y. Huang, L. Zhang, Y. Zhang, R. Jia, *J. Alloys Compd.* 798 (2019) 458.
- [24] D.Y. Guo, H.Z. Shi, Y.P. Qian, M. Lv, P.G. Li, Y.L. Su, Q. Liu, K. Chen, S.L. Wang, C. Cui, C.R. Li, W.H. Tang, *Semicond. Sci. Technol.* 32 (2017): 03LT01.
- [25] W.Y. Kong, G.A. Wu, K.Y. Wang, T.F. Zhang, Y.F. Zou, D.D. Wang, L.B. Luo, *Adv. Mater.* 28 (48) (2016) 10725–10731.
- [26] B. Zhao, F. Wang, H. Chen, L. Zheng, L. Su, D. Zhao, X. Fang, *Adv. Funct. Mater.* 27 (17) (2017): 1700264.
- [27] M. Chen, B. Zhao, G. Hu, X. Fang, H. Wang, L. Wang, J. Lou, X. Han, Z.L. Wang, *Adv. Funct. Mater.* 28 (14) (2018): 1706379.
- [28] D.Y. Guo, Y.L. Su, H.Z. Shi, P.G. Li, N. Zhao, J.H. Ye, S.L. Wang, A.P. Liu, Z. Chen, C. Li, W.H. Tang, *ACS Nano* 12 (2018) 12827.
- [29] D.Y. Guo, Z.P. Wu, P.G. Li, Y.H. An, H. Liu, X. Guo, H. Yan, G. Wang, C. Sun, L. Li, W.H. Tang, *Opt. Mater. Express* 4 (2014) 1067.
- [30] D.Y. Guo, Z.P. Wu, Y.H. An, P.G. Li, P.C. Wang, X.L. Chu, X.C. Guo, Y.S. Zhi, M. Lei, L.H. Li, W.H. Tang, *Appl. Phys. Lett.* 106 (2015): 042105.
- [31] S. Ahn, F. Ren, S. Oh, Y. Jung, J. Kim, M.A. Mastro, J.K. Hite, C.R.E. Jr, S.J. Pearson, *J. Vac. Sci. Technol. B*, 34 (2016): 041207.
- [32] S. Luan, L. Dong, X. Ma, R. Jia, *J. Alloys Compd.* 812 (2019): 152026.
- [33] D.Y. Guo, Y.H. An, W. Cui, Y. Zhi, X. Zhao, M. Lei, L. Li, P.G. Li, Z.P. Wu, W.H. Tang, *Sci. Rep.* 6 (2016) 25166.
- [34] L. Dong, J. Yu, Y. Zhang, R. Jia, *Comput. Mater. Sci.* 156 (2019) 273.
- [35] M. Marezio, J.P. Remeika, *J. Chem. Phys.* 46 (1967) 1862.
- [36] V.M. Bermudez, *Chem. Phys.* 323 (2006) 193.
- [37] H.Y. Playford, A.C. Hannon, M.G. Tucker, D.M. Dawson, S.E. Ashbrook, R.J. Kastabin, J. Sloan, R.I. Walton, *J. Chem. Phys. C* 118 (2014) 16188.
- [38] S. Yoshioka, H. Hayashi, A. Kuwabara, F. Oba, K. Matsunaga, I. Tanaka, *J. Phys. Condens. Matter* 19 (2007): 346211.
- [39] L.P. Dong, J.G. Yu, Y.M. Zhang, R.X. Jia, *Comput. Mater. Sci.* 156 (2019) 273.
- [40] D. Shinohara, S. Fujita, Jpn. J. Appl. Phys. 47 (2008) 7311.
- [41] H.Y. Playford, A.C. Hannon, E.R. Barney, R.I. Walton, *Chem. Eur. J.* 19 (2013) 2803.
- [42] C.R. He, D.Y. Guo, K. Chen, S.L. Wang, J.Q. Shen, N. Zhao, A.P. Liu, Y. Zheng, P.G. Li, Z.P. Wu, C. Li, F.M. Wu, W.H. Tang, *ACS Appl. Nano Mater.* 2 (2019) 4095.
- [43] X.C. Guo, N.H. Hao, D.Y. Guo, Z.P. Wu, Y.H. An, X.L. Chu, L.H. Li, P.G. Li, M. Lei, W.H. Tang, *J. Alloys Compd.* 660 (2016) 136.
- [44] X.T. Cao, X. Cao, H.J. Guo, T. Li, Y. Jie, N. Wang, Z.L. Wang, *ACS Nano* 10 (8) (2016) 8038–8044.
- [45] Z.N. Wang, R.M. Yu, X.F. Wang, W.Z. Wu, Z.L. Wang, *Adv. Mater.* 28 (32) (2016) 6880–6886.
- [46] M.-G. Ju, X. Wang, W. Liang, Y. Zhao, C. Li, *J. Mater. Chem. C* 2 (2014) 17005.
- [47] R. Lin, W. Zheng, D. Zhang, Z. Zhang, Q. Liao, L. Yang, F. Huang, *ACS Appl. Mater. Interfaces* 10 (2018) 22419.
- [48] M.L. Ai, D.Y. Guo, Y. Qu, W. Cui, Z.P. Wu, P.G. Li, L. Li, W.H. Tang, *J. Alloys Compd.* 692 (2017) 634.
- [49] I.H. Abidi, Y. Liu, J. Pan, A. Tyagi, M. Zhuang, Q. Zhang, A.A. Cagang, L.-T. Weng, P. Sheng, W.A. Goddard, Z. Luo, *Adv. Funct. Mater.* 27 (2017): 1700121.
- [50] J. Baltazar, H. Sojoudi, S.A. Paniagua, S. Zhang, R.A. Lawson, S.R. Marder, S. Graham, L.M. Tolbert, C.L. Henderson, *Adv. Funct. Mater.* 24 (2014) 5147.
- [51] X. Wan, K. Chen, Z. Chen, F. Xie, X. Zeng, W. Xie, J. Chen, J. Xu, *Adv. Funct. Mater.* 27 (2017): 1603998.
- [52] S. Liu, Q. Liao, S. Lu, Z. Zhang, G. Zhang, Y. Zhang, *Adv. Funct. Mater.* 26 (2016) 1347.
- [53] S. Lin, H. Wang, F. Wu, Q. Wang, X. Bai, D. Zu, J. Song, D. Wang, Z. Liu, Z. Li, N. Tao, K. Huang, M. Lei, B. Li, H. Wu, *NPJ Flex. Electron.* vol. 3 (2019).
- [54] S. Lin, H. Wang, X. Zhang, D. Wang, D. Zu, J. Song, Z. Liu, Y. Huang, K. Huang, N. Tao, Z. Li, X. Bai, B. Li, M. Lei, Z. Yu, H. Wu, *Nanomater. Energy* 62 (2019) 111.
- [55] Y.C. Chen, Y.J. Lu, C.N. Lin, Y.Z. Tian, C.J. Gao, L. Dong, C.X. Shan, *J. Mater. Chem. C* 6 (2018) 5727.
- [56] Y. Qu, Z.P. Wu, M.L. Ai, D.Y. Guo, Y.H. An, H. Yang, L. Li, W.H. Tang, *J. Alloys Compd.* 680 (2016) 247.
- [57] W. Zheng, Z.J. Zhang, R.C. Lin, K. Xu, J. He, F. Huang, *Adv. Electron. Mater.* 2 (2016): 1600291.
- [58] W. Zheng, F. Huang, R. Zheng, H. Wu, *Adv. Mater.* 27 (2015) 3921–3927.
- [59] M.L. Ai, D.Y. Guo, Y.Y. Qu, W. Cui, Z.P. Wu, P.G. Li, L.H. Li, W.H. Tang, *J. Alloys Compd.* 692 (2017) 634.
- [60] D.Y. Guo, H.Z. Shi, Y.P. Qian, M. Lv, P.G. Li, Y.L. Su, Q. Liu, K. Chen, S.L. Wang, C. Cui, C.R. Li, W.H. Tang, *Semicond. Sci. Technol.* 3 (32) (2017): 03lt01.